

Article

Photoreduction of a Pd-Doped Mesoporous TiO₂ Photocatalyst for Hydrogen Production under Visible Light

Bianca Rusinque, Salvador Escobedo  and Hugo de Lasa *

Chemical Reactor Engineering Centre (CREC), Faculty of Engineering, Western University, London, ON N6A 5B9, Canada; brusinqu@uwo.ca (B.R.); selfa.iq@gmail.com (S.E.)

* Correspondence: hdelasa@uwo.ca; Tel.: +1-519-661-2149

Received: 16 November 2019; Accepted: 27 December 2019; Published: 3 January 2020



Abstract: Photoreduction with visible light can enhance the photocatalytic activity of TiO₂ for the production of hydrogen. In this article, we present a strategy to photoreduce a palladium-doped TiO₂ photocatalyst by using near-UV light prior to its utilization. A sol-gel methodology was employed to prepare the photocatalysts with different metal loadings (0.25–5.00 wt% Pd). The structural and morphological characteristics of the synthesized Pd-TiO₂ were analyzed by using X-ray Diffraction (XRD), BET Surface Area (S_{BET}), Temperature Programmed Reduction (TPR), Chemisorption and X-ray Photoelectron Spectroscopy (XPS). Hydrogen was produced by water splitting under visible light irradiation using ethanol as an organic scavenger. Experiments were developed in the Photo-CREC Water-II (PCW-II) Reactor designed at the CREC-UWO (Chemical Reactor Engineering Centre). It was shown that the mesoporous 0.25 wt% Pd-TiO₂ with 2.5 eV band gap exhibits, under visible light, the best hydrogen production performance, with a 1.58% Quantum Yield being achieved.

Keywords: photoreduction; palladium; TiO₂; hydrogen production; visible light; photocatalysis quantum yield; Photo-CREC Water II Reactor

1. Introduction

In the last few years, researchers have been investigating clean and emission-free renewable energy resources [1]. In this respect, hydrogen is an energy vector that has attracted the attention of many scientists in both academia and industry [2–7]. Hydrogen is one of the most abundant elements on earth that can be obtained from a variety of organic sources [8]. Besides its abundance, hydrogen has a high calorific value (143 MJ/kg) and clean emissions, with the combustion of hydrogen producing water as the only by-product [9,10].

Photocatalysis provides a promising method for hydrogen production [11]. This method involves photons and semiconductors that generate electron-hole pairs, facilitating water splitting [12]. Photoexcited electron-hole pairs can be separated efficiently using sacrificial agents, which allow the formation of hydrogen with reduced electron-hole pair recombination [13–17]. Nowadays, however, this process faces challenges in being implemented using visible light, given its low photon conversion efficiency [18].

In order to achieve photocatalytic water splitting, feasible photocatalysts must meet the following criteria: (a) They must display suitable band gaps to absorb visible light, (b) They must be chemically stable under redox conditions, (c) They must have a low cost, (d) They must be recyclable, (e) They must be chemically resistant and (f) They must be adaptable for large-scale hydrogen production [19,20].

Until today, synthesized titanium dioxide (TiO₂) has been the most frequently used semiconductor due to its oxidation and chemical resistance properties, accessibility, and affordability [21]. TiO₂

contains three allotropic phases: anatase, rutile, and brookite [22]. However, anatase appears to be the most desirable phase for photocatalytic hydrogen production [23]. Synthesized mesoporous semiconductors may also add significant beneficial features to photocatalysis given that they may contribute with: (a) favorable electronic structures, (b) adequate properties for light absorption, (c) sufficient electron transport properties, (d) good photo-semiconductor excitation and (e) suitable chemical species transport properties [24].

Photocatalytic reactions can be realized via sunlight irradiation [25]. TiO₂ is however, limited by its 3.2 eV band gap, being able the use about 4% of the solar spectrum only. Thus, modified TiO₂-based photocatalysts with smaller band gaps are required for more efficient sunlight utilization [26]. One possible approach to modify photocatalysts is by loading a noble metal as a co-catalyst. For instance, it has been proven that loading a noble metal on TiO₂ is an effective method to improve its photoactivity [27]. In this respect, in prior studies, our group has investigated the effect of platinum on TiO₂ under near-UV light [28,29].

Nevertheless, one can consider the use of less expensive noble metal co-catalysts with lower Fermi levels than TiO₂, such as palladium. In this respect, palladium is anticipated to decrease the electron-hole recombination, leading to an energy band gap reduction [30]. Abdelaal et al. [31], for instance, prepared a Pd-TiO₂ photocatalyst for methylene blue degradation under a 300 W Xenon lamp irradiation. Once the Pd metal was added, authors observed a diminished band gap of 3.04 eV. Likewise, Espino et al. [32], doped TiO₂ with palladium for sodium diclofenac, isoproturon, and phenol degradation in water using a 400 W mercury lamp. They noticed a decreased band gap of 2.78 eV.

In the present study, a mesoporous Pd-TiO₂ photocatalyst active under visible light is considered. A key preparation step, photoreducing the Pd-TiO₂ using near-UV light is implemented to enhance its photocatalyst activity [33]. It is shown, that the near-UV light photoreduced mesoporous Pd-TiO₂ displays a 2.51 eV energy band gap. The near-UV light photoreduced Pd-TiO₂ photocatalyst is evaluated in a Photo-CREC Water-II Reactor (PCW-II Reactor) under visible light [34]. Ethanol is employed as an organic scavenger to help with electron-hole separation [33]. The promoted mesoporous Pd-TiO₂ energy band gap reduction enhances light absorption in the visible region [35]. This leads as is reported in the present study, to enhanced hydrogen production and increased Quantum Yields (QY).

2. Results and Discussion

2.1. Photocatalyst Characterization

2.1.1. Adsorption-Desorption Isotherms

The BET-surface area (S_{BET}), the pore diameter (D_p), and the pore volume (V_p) of the prepared photocatalysts are reported in Table 1. These mesoporous photocatalysts display an increase in the specific surface area versus the one obtained for Degussa P-25. For the TiO₂ doped with palladium in amounts greater than 0.25 wt%, a decrease in the specific surface area and an increase in the average pore diameter were noticed, with this being attributed to a moderate blocking of the TiO₂ pores with Pd [36].

Table 1. Surface Area, Pore Diameter, and Pore Volume of the Prepared Photocatalysts.

Photocatalyst	S_{BET} (m ² g ⁻¹)	D_p^{BJH} (4 $V_p^{\text{BJH}}/S_{\text{BET}}$) (nm)	V_p^{BJH} (cm ³ g ⁻¹)
DP-25	59	7.5	0.11
TiO ₂	140	17.5	0.61
0.25 wt% Pd-TiO ₂	131	16.5	0.53
0.50 wt% Pd-TiO ₂	124	16.8	0.52
1.00 wt% Pd-TiO ₂	123	21.2	0.65
2.50 wt% Pd-TiO ₂	122	19.9	0.60
5.00 wt% Pd-TiO ₂	119	18.9	0.56

On the other hand, and when utilizing the Barrett–Joyner–Halenda (BJH) methodology, the mesoporous pore size distribution was found to be unimodal for the 0.25 and 0.50 wt% Pd–500 °C thermally treated TiO₂ photocatalysts, with pore sizes in the 18–22 nm range. However, and for the photocatalysts with Pd loadings equal or larger than 1.0 wt%, the unimodal pore size distribution evolved towards a bimodal pore size distribution, with a second peak at 16–35 nm.

2.1.2. Hydrogen Chemisorption

By employing hydrogen pulse chemisorption, it was possible to determine the fraction of dispersed Pd on the photocatalyst [37]. Specifically, by assuming that only one hydrogen molecule chemisorbs on a single Pd site, the metal percent dispersion was calculated as reported in Table 2. This shows that increasing the metal loading decreases the metal dispersion, with the metal loading remaining at a high 75% for the 0.25 wt% Pd–TiO₂.

Table 2. Metal Dispersion on TiO₂ Photocatalysts.

Photocatalyst	Metal Dispersion (%)
0.25 wt% Pd–TiO ₂	75
0.50 wt% Pd–TiO ₂	27
1.00 wt% Pd–TiO ₂	26
2.50 wt% Pd–TiO ₂	12
5.00 wt% Pd–TiO ₂	8

2.1.3. X-ray Diffraction (XRD)

The mass fractions of anatase and rutile were determined from the relative XRD diffraction band intensities, using an anatase sample with a 100% TiO₂ crystalline phase as a reference [25]. XRD patterns obtained for the different photocatalysts, are shown in Figure 1. XRD peaks for DP25, anatase and rutile are also given in Figure 1 in order to compare them with those of the Pd–TiO₂ photocatalysts. XRD peaks at 25°, 38°, 48°, 54°, 63°, 69°, 70.5° and 75° 2θ diffraction angles were assigned to anatase (101), (004), (200), (105), (204), (116), (220) and (215) crystal planes [JCPDS No. 73-1764], whereas XRD peaks at 40.12° and 46.66° were assigned to Pd (111) and (200) crystalline planes, respectively [JCPDS No. 87-0638].

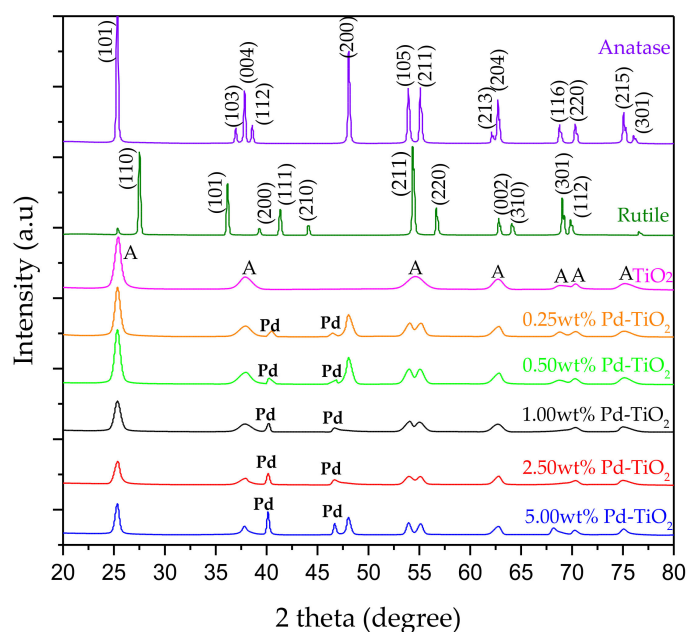


Figure 1. X-ray Diffractograms for Pd-Doped TiO₂ Photocatalysts. XRDs for A = anatase and Pd = palladium are shown as a reference.

Figure 2 reports a comparative analysis of the XRD diffractograms for the photocatalysts before and after reduction. One can see a peak at 34° of the 2θ angle scale, which corresponds to (002) reflections of a tetragonal palladium oxide phase [JCPDS 41-1107]. Furthermore, the peaks at 40° and 46° of the 2θ angle scale relate to the Pd° [JCPDS No. 87-0638]. Thus, there is a structural difference in the semiconductor material after the reduction process, with the absence of XRD detectable palladium oxides and the formation of metallic palladium $h k l$ (1 1 1) and (2 0 0).

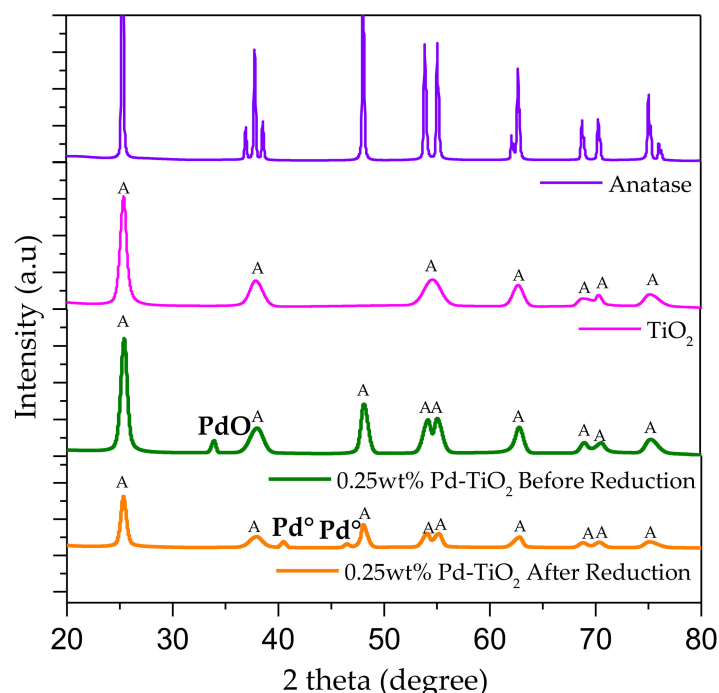


Figure 2. Comparative Analysis of 0.25 wt% Pd-TiO₂ Photocatalysts Before and After Reduction. A = anatase, PdO = palladium oxide and Pd[°] = metallic palladium.

Furthermore, the average size of the crystallites was calculated based on XRD peak broadening using the Scherrer Equation. The calculated crystallite sizes were between 9 and 14 nm and they are reported in Table 3.

Table 3. Photocatalyst Crystallite Sizes.

Photocatalyst	Crystallite Size (nm)
DP 25	21
TiO ₂	9
0.25 wt% Pd -TiO ₂	11
0.50 wt% Pd -TiO ₂	11
1.00 wt% Pd -TiO ₂	11
2.50 wt% Pd -TiO ₂	13
5.00 wt% Pd -TiO ₂	14

Additionally, the lattice constants of the tetragonal anatase unit cells were calculated for the anatase phase ($h k l$) = (1 0 1). The resulting $a = b = 3.7779$ and $c = 3.4888$ parameters at 25° in the 2θ angle scale, showed that pure anatase was present in the photocatalysts [38].

2.1.4. Temperature Programmed Reduction (TPR)

Temperature Programmed Reduction (TPR) is one key parameter that could influence photocatalyst performance. TPR showed that once the photocatalyst was under hydrogen flows, the palladium oxide

species were reduced [39], with four TPR peaks being observed. The first negative peak at 68 °C was attributed to the decomposition of palladium β -hydride, which occurred as soon as the hydrogen and palladium came into contact, at the beginning of the analysis. This negative peak at 68 °C may be larger at higher Pd loadings in excess of 0.25 wt% [40], with this being attributed to the higher Pd dispersions. The second broad peak was assigned to palladium oxide reduction. This peak started at 200 °C and was completed at 300 °C. This broad peak was attributed to the broad palladium particle size distribution (18–22 nm) [41], with larger particle sizes moderately increasing the palladium oxide reduction temperature.

Furthermore, as reported in Figure 3, the 0.25 wt%Pd-TiO₂ semiconductor showed double peaks in the 400–600 °C range, which were attributed to the Ti⁺⁴ ions surface reduction [42]. Similar trends to the ones reported in Figure 3 were found for all doped photocatalysts, with these consisting of 0.25 wt% to 5.00 wt% Pd-TiO₂. It should be noted, however, that only the second peak in the 200–300 °C range was considered in all the calculations, in order to establish the amount of reducible palladium.

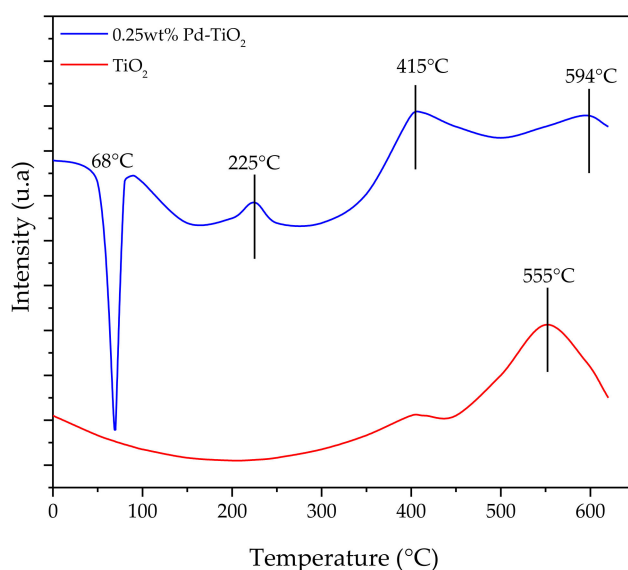


Figure 3. Temperature Programmed Reduction (TPR) of TiO₂ and 0.25 wt% Pd-TiO₂.

In summary, one can see that for the Pd-TiO₂ of the present study, the Pd reduction temperature was above 350 °C, which suggests strong metal-support interactions, potentially leading to high photocatalytic hydrogen production activity [43].

2.1.5. Band Gap

Figure 4 illustrates the UV-visible absorption spectra of the Pd-TiO₂ at different metal loadings while applying the Kubelka–Munk (K–M) model, following the Tauc plot methodology. When using the Kubelka–Munk (K–M) method, the band gap is determined by drawing a straight line in the $(\alpha h\nu)^{0.5}$ versus $(h\nu)$ plot with α representing the absorption coefficient, h being the Planck constant (6.64×10^{-34} J s/photon) and ν denoting the radiation frequency [44]. Following this, the location of the band gap is determined at the straight line intersection with the x-axis. Figure 4 reports the Tauc plots of the doped TiO₂ with 0.25 wt%Pd, 0.5 wt%Pd, 1 wt%Pd, 2.5 wt%Pd, and 5 wt%Pd loadings.

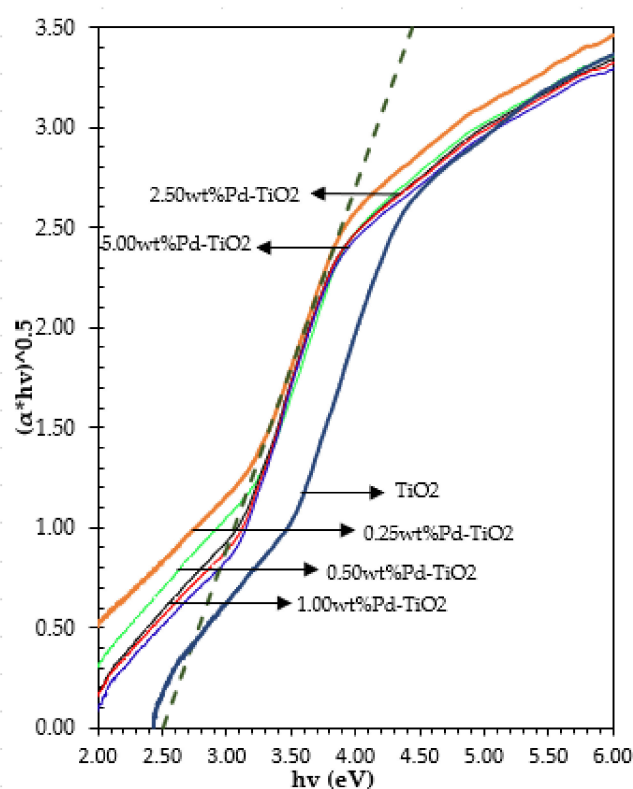


Figure 4. Band Gap Calculation Using the Tauc Plot Methodology. A straight-line extrapolation is shown for the 0.25 wt% Pd-TiO₂.

For instance, one can observe in Figure 4, that for the 0.25 wt% Pd-TiO₂, a linear extrapolation yields a 2.51 eV band gap. This 2.51 eV band gap corresponds to a 494 nm photon wavelength (λ) given $\lambda = hc/E_{bg}$, with h being the Planck constant (6.34×10^{-34} J s/photon), c being the speed of light under vacuum (3.00×10^8 m/s²), and E_{bg} being the electron band gap. One should note, that 2.51 eV represents a significantly reduced E_{bg} with respect to the 2.99 eV band gap for mesoporous TiO₂ without Pd, as reported in Table 4. It is also observed in Table 4 that using Pd loadings above 0.25 wt%, yields to a reversed trend in the E_{bg} , with band gaps increasing steadily instead.

Table 4. Photocatalysts Band Gaps.

Photocatalyst	Band Gap (eV)
DP-25	3.10
TiO ₂	2.99
0.25 wt% Pd-TiO ₂	2.51
0.50 wt% Pd-TiO ₂	2.55
1.00 wt% Pd-TiO ₂	2.60
2.50 wt% Pd-TiO ₂	2.67
5.00 wt% Pd-TiO ₂	2.67

In this respect, one could assign the band gap decrease of the 0.25 wt% Pd-TiO₂ to the Fermi level changes. These changes can be assigned to the sp-d orbital exchange interactions between the band electrons and the localized d electrons of the Pd 3d ions substituting the Ti⁴⁺ cations. The s-d and p-d exchange interactions give rise to a downward shift of the conduction band edge and an upward shift of the valence band edge, leading to a band gap narrowing [45–48]. However, at higher than 0.25%wt Pd loadings, it is speculated that the band gap increase is due to the dominant d-d transitions over the sp-d transitions.

Thus, one can consider, that low noble metal loadings (e.g., 0.25%wt Pd-TiO₂) facilitate both charge collection and light absorption [49]. Low Pd loadings give rise to localized energy levels in the band gap of the TiO₂. In this case, the valence band electrons of the TiO₂ are excited at wavelengths longer than 400 nm [50]. Alternatively, excessive noble metal loading may lead to smaller photocatalyst specific surface areas, with larger metal crystallites formed with PdO inclusions [51]. In this respect, XPS confirmed that the PdO presence shields incident photons, blocking light absorption and preventing the generation of semiconductor electron-hole pairs [52].

2.1.6. X-ray Photoelectron Spectroscopy (XPS)

For chemical state identification, quantitative XPS analyses were performed on: a) 0.25 wt%–5 wt% Pd-TiO₂ before photoreduction and b) 0.25%Pd-TiO₂ after photoreduction. The Pd 3d_{3/2} and Pd 3d_{5/2} spin orbital splitting photoelectrons were observed in both the photoreduced and non-photoreduced 0.25 wt% Pd-TiO₂ photocatalysts.

Figure 5 reports the photoreduced and non-photoreduced 0.25 wt% Pd-TiO₂ photocatalyst XPS peaks. XPS peaks were analyzed via band deconvolution, at the 334.54 eV, 336.38 eV, 339.69 eV, and 341.54 eV characteristic binding energies.

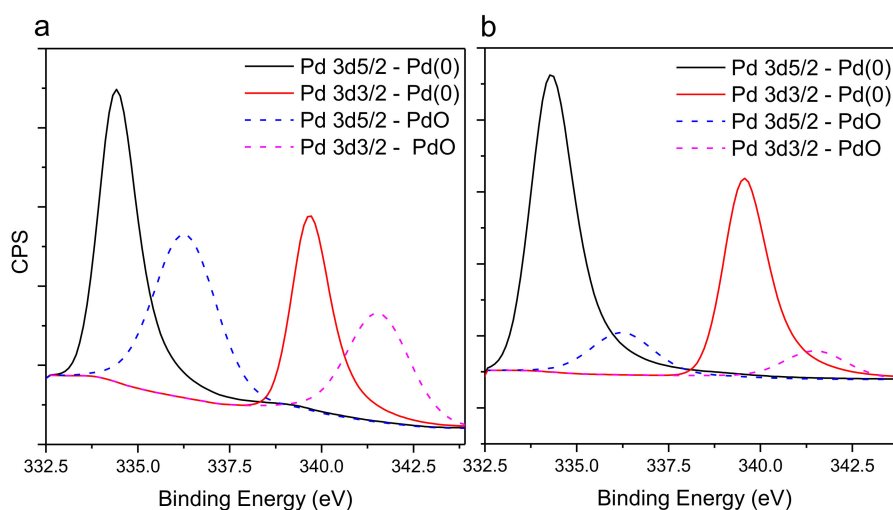


Figure 5. High-Resolution X-ray Photoelectron Spectroscopy (XPS) Spectra for 0.25 wt% Pd-TiO₂: (a) Before photoreduction and (b) After photoreduction. Note: Continuous lines represent Pd⁰ at (i) 3d_{5/2} and (ii) 3d_{3/2}. Broken lines represent PdO at (iii) 3d_{5/2} and (iv) 3d_{3/2}.

Table 5 reports the observed binding energies for the 0.25 wt% Pd-TiO₂ with the full-widths-at-half-maximum (FWHM) and percentual areas.

Table 5. High-Resolution X-ray Photoelectron Spectroscopy (XPS) Spectra Binding Energies and Peak Areas for the 0.25 wt% Pd-TiO₂.

Peak Name	Before Photoreduction			After 60 min of Photoreduction Using Near-UV Irradiation		
	Binding Energy	FWHM	% Area	Pos	FWHM	% Area
Pd 3d _{3/2} PdO	341.54	2.00	50.2	341.49	2.00	18.3
Pd 3d _{3/2} Pd ⁰	339.69	1.13	49.8	339.56	1.29	81.7
Pd 3d _{5/2} PdO	336.28	2.00	50.2	336.23	2.00	18.3
Pd 3d _{5/2} Pd ⁰	334.43	1.13	49.8	334.30	1.29	81.7

Thus, one can see that according to Table 5 and Figure 5, the 0.25 wt% Pd–TiO₂ photocatalyst displays in the XPS, the two most intense peaks, at 334.43 and 339.69 eV. These peaks are assigned to the metallic Pd. Furthermore, there are two other weaker recorded peaks at 336.28 and 341.54 eV, which are attributed to 3d5/2 and 3d3/2 binding energies of the PdO species.

Table 5 reports a comparison between the XPS binding energies of the 0.25 wt% Pd–TiO₂ photocatalyst before and after 60 min. of near-UV photoreduction. One can see that there is a significantly increased in Pd⁰ content ranging from 49.8% up to 81.7% after UV irradiation, with the remaining PdO amounting to 18.3% only. This increased Pd⁰ is the result of near-UV electrons diminishing the oxidized Pd species.

Furthermore, the XPS analysis of the 0.25%wt Pd-TiO₂ photocatalysts, also showed Ti 2p and O 1s bands at peaks of 454 and 526 eV, respectively (not displayed). These bands were assigned to the titanium oxide.

2.2. Macroscopic Irradiation Energy Balance (MIEB)

The MIEB were developed in a carefully selected 6000 cm³ Photo-CREC Water-II Reactor control volume. This control volume as described in Figure 6, contained uniformly suspended Pd-TiO₂ photocatalysts.

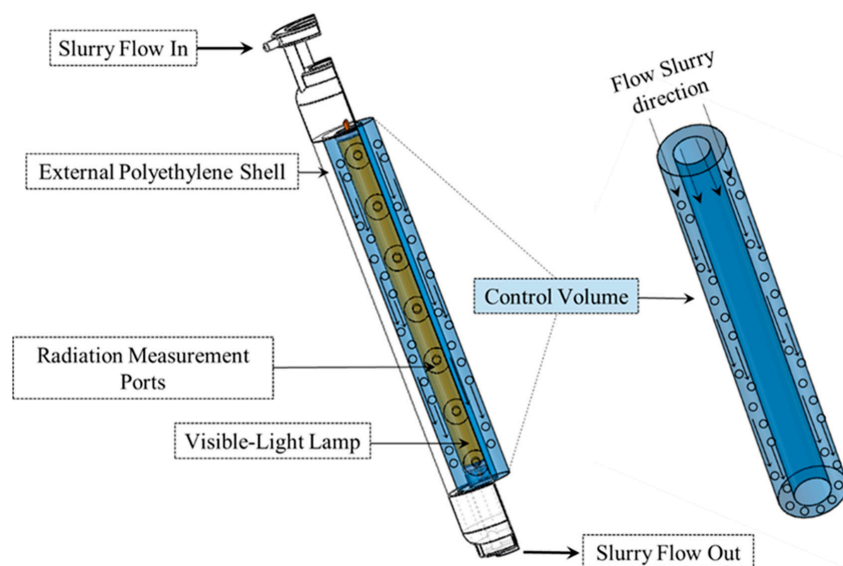


Figure 6. Schematic Representation of the 6000 cm³ Slurry Control Volume Involved in the Macroscopic Radiation Balances.

On this basis, the rate of photon absorption was calculated as [27]:

$$P_a = P_i - P_{bs} - P_t \quad (1)$$

where, P_a = the rate of absorbed photons, P_i = the rate of photons reaching the reactor inner surface, P_{bs} = the rate of backscattered photons exiting the system, and P_t = the rate of transmitted photons in Einstein/s. It is desirable to obtain a high rate of absorbed photons for photocatalytic processes. For detailed calculations of the MIEB refer to Appendix A.

The P_a (rate of absorbed photons) was calculated as shown in Table 6. One can thus see, that when a 0.25 wt% Pd-TiO₂ is used, there is a significant P_a increase versus the P_a value when undoped TiO₂ is utilized. However, one can also observe that larger loadings than 0.25 wt% Pd on TiO₂ yield a mildly increased P_a with 1.00 wt% Pd on TiO₂ giving a P_a maximum. Larger than 1.00 wt% Pd on TiO₂ yield a modest P_a decrease, with a consequently diminishing absorption efficiency.

Table 6. Rates of Absorbed Photons on the Photocatalysts of this study using a Consistent 0.15 g/L Photocatalyst Loading. All photocatalysts doped with Pd were photoreduced for 60 min. prior to their utilization. P_i is estimated to be 9.54×10^{-6} Einstein/s.

Catalyst Loading	P_a (Einstein/s)
TiO ₂	2.23×10^{-6}
0.25 wt% Pd - TiO ₂	4.37×10^{-6}
0.50 wt% Pd- TiO ₂	4.45×10^{-6}
1.00 wt% Pd- TiO ₂	5.62×10^{-6}
2.50 wt% Pd- TiO ₂	4.87×10^{-6}
5.00 wt% Pd- TiO ₂	4.81×10^{-6}

In summary, TiO₂ photocatalysts doped with Pd considerably augment the absorbed visible irradiation photons, and this is the case when compared to the undoped TiO₂.

2.3. Hydrogen Production

The Pd-TiO₂ photocatalysts of the present study were evaluated in the PCW-II with respect to their ability to enhance hydrogen production, under the following conditions: (a) by utilizing a photocatalyst concentration of 0.15 g/L, (b) by using a 2.0 v/v% of ethanol as organic scavenger and (c) by utilizing a pH = 4 ± 0.05 .

Figure 7 reports the cumulative hydrogen volume produced, using TiO₂ doped with different Pd loadings under visible light. It was shown that Pd-TiO₂ semiconductors consistently enhance hydrogen production, with the best performance obtained with the 0.25 wt% Pd. This mesoporous semiconductor may have an increased scavenging effect of photogenerated electrons and therefore, prevent electron–hole pairs recombination [53].

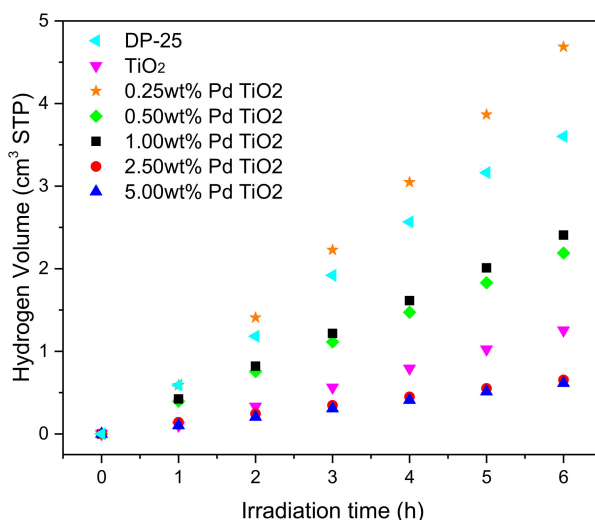


Figure 7. Cumulative Hydrogen Volume Using Pd-TiO₂ photocatalysts with Different Metal Loadings (0.25, 1.50, 1.00, 2.50 and 5.00 wt%). Conditions: photocatalyst concentration 0.15 g/L, 2.0 v/v% ethanol, pH = 4 ± 0.05 and visible light. Note: The experimental data reported is the result of 4 consecutive runs, each lasting 6 h. Standard deviation for repeats were $\pm 4.3\%$.

Furthermore, it was also observed that when the metal loading of the Pd-TiO₂ was augmented to 0.5 wt% Pd and above, a decreased rate of hydrogen production was obtained. One should notice as well, that the MIEB as reported in Table 6, showed relatively stabilized visible light absorption for various Pd doped TiO₂ photocatalysts. Thus, one can conclude that hydrogen production differences cannot be assigned to changes in electron and hole pairs generation [54], but rather to a most effective trapping of electrons in 0.25 wt%Pd-TiO₂ than in photocatalysts with larger Pd loadings.

Figure 6 also displays that after only 6 h of visible light irradiation, a maximum volume of 4.7 cm³ STP (standard temperature and pressure) of hydrogen is obtained when using the 0.25 wt% Pd on TiO₂. This volume is approximately 4 times higher than the volume produced with undoped mesoporous TiO₂.

2.3.1. Precursor Near UV-Light Photoreduction

Palladium is present in a metallic state during the sol-gel photocatalyst preparation. However, palladium can be oxidized during the photocatalyst precursor calcination preparation step. Confirmation of this is given by the X-ray Diffraction Analysis where at 34° (111) of the 2θ angle scale, there is indication of the presence of PdO. As well, the XPS also shows that 50.2% of palladium is present as PdO after photocatalyst precursor calcination as reported in Table 5. Thus and on this basis, one can conclude that palladium species on the semiconductor requires further reduction, to ensure that a substantial amount of palladium species is present as Pd⁰.

Therefore, a special and additional photocatalyst pretreatment was implemented in the present study, to ensure that most palladium was appropriately reduced to Pd⁰. Pd⁰ promotes the high photocatalytic activity of TiO₂, by generating a Schottky junction between the metal and the photocatalyst. The metal particles trap and store the photogenerated electrons, reducing the rate of the electron hole recombination [55].

With this end and as described in Figure 8, a 15W BLB UV-Lamp was employed to irradiate the prepared semiconductor during 1 h.

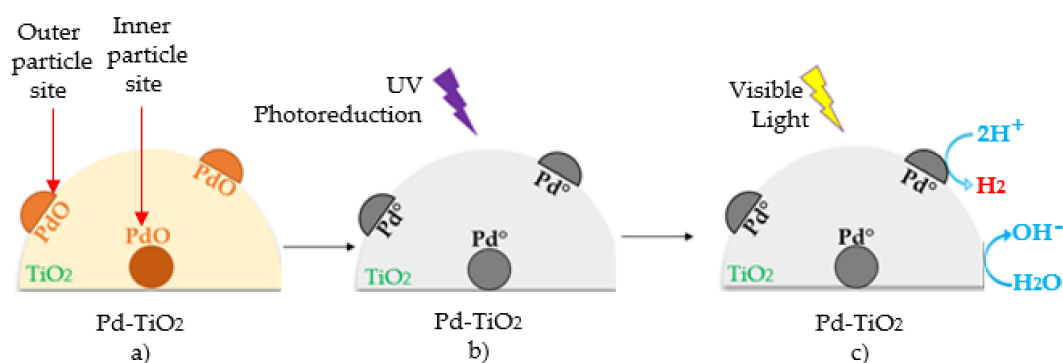


Figure 8. Schematic Representation of: (a) The synthesized photocatalysts following calcination at 500 °C with most of the Pd being present as PdO, (b) The photoreduction of the PdO to Pd⁰ using a UV-Lamp for 1 h, (c) The H₂ production using a photoreduced Pd-TiO₂, with molecular H₂ being generated on the semiconductor.

This PdO photoreduction using near UV light can be described as per Equation (2), with the resulting palladium being present as Pd⁰ on the TiO₂ structure.



It is speculated that photoreduction as per Equation (2), is a very efficient process with photogenerated electrons migrating from the outer TiO₂ particle surface to the TiO₂ mesoporous inner surface. Formed electrons can reduce the PdO into Pd⁰ [56].

Regarding the present studies, following photoreduction, the near-UV lamp was replaced by a visible light lamp. It was then observed that when the photocatalyst was photoreduced prior to its utilization, this led to an important increase in hydrogen production, under visible light irradiation.

Figure 9 displays an enhanced cumulative hydrogen production under visible light in the Photo-CREC Water Reactor II at different loadings (0.25, 0.50, 1.00, 2.50 and 5.00 wt%). It is interesting to see that the same consistent trends were observed in previous studies of our research team,

using near-UV light [57]. It has to be noted as well, that the lower the Pd loadings, the higher the hydrogen production.

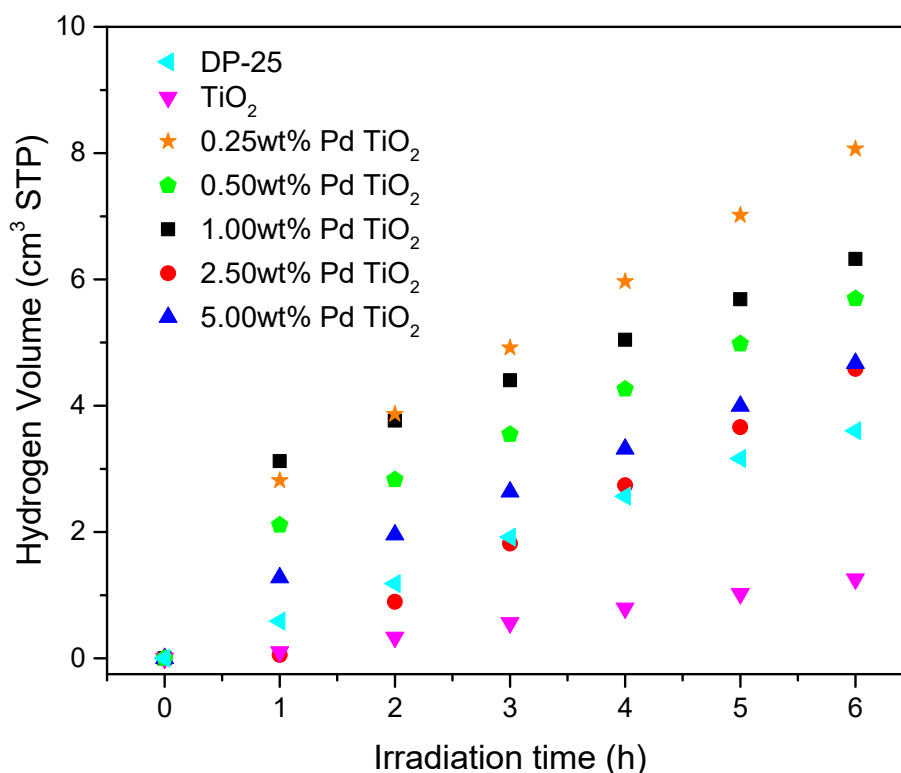


Figure 9. Cumulative Hydrogen Volume at Different 0.25, 0.50, 1.00, 2.50 and 5.00 wt% Pd Loadings utilizing a photoreduced photocatalyst after UV light exposure. Conditions: Photocatalyst concentration: 0.15g/L, 2.0 v/v% ethanol, pH = 4 ± 0.05. Experimental data is the result of 4 consecutive runs for each photocatalyst.

Furthermore, when comparing Figures 7 and 9, it can be observed that the photoreduced Pd-TiO₂ photocatalyst displayed significantly increased hydrogen production rates. Particularly for the 0.25 wt% Pd-TiO₂ after photoreduction, the maximum hydrogen volume produced was 8.0 cm³ STP. This is equivalent to a 1.7 times increased hydrogen production rate. At this low palladium loading, a good metal dispersion of 75% was also observed, according to the chemisorption studies, with a slightly decreased surface area and average pore size [58].

In contrast, when using the 0.50 and 5.00 wt% Pd-TiO₂, lower metal dispersions were observed, with larger metal crystallite sizes being detected. This was in line with their diminished photocatalytic hydrogen production activity [59]. To explain these results, one can consider that under visible light and using a Pd-TiO₂ photocatalyst, photons are both absorbed and scattered. The MIEB as reported in Section 2.2, showed that higher Pd loadings (2.5 and 5.0 wt% Pd) do not enhance the absorption of visible light significantly. This phenomenon can be assigned to the presence of larger metal crystallites and TiO₂ particle agglomerates. This limits photons from reaching the Pd⁰ active metallic sites and from being absorbed [60]. The opposite of this was observed at lower than 1.00 wt% Pd loadings, where the photon absorption increases, positively impacting the semiconductor photoactivity.

On the other hand, it can be hypothesized as well, that the less effective photoreduction of palladium may occur for 2.5 and 5.0 wt% Pd on TiO₂, due to the oversupply of noble metal. In this case, layers of PdO could still be present on the TiO₂, shielding the TiO₂ from light absorption. The formation of such sites could increase the photocatalyst reflectivity leading to visible light scattering [61]. As well, this phenomenon could also be attributed to the partial blocking of semiconductor pores, which may decrease the TiO₂ specific surface area, as reported in Table 1.

Given that hydrogen is produced under visible light, the photogenerated holes created by the noble metal react with the organic scavenger ethanol forming byproducts such as acetaldehyde, ethane, CO₂ and methane, in a progressive increment as is shown in Figure 10.

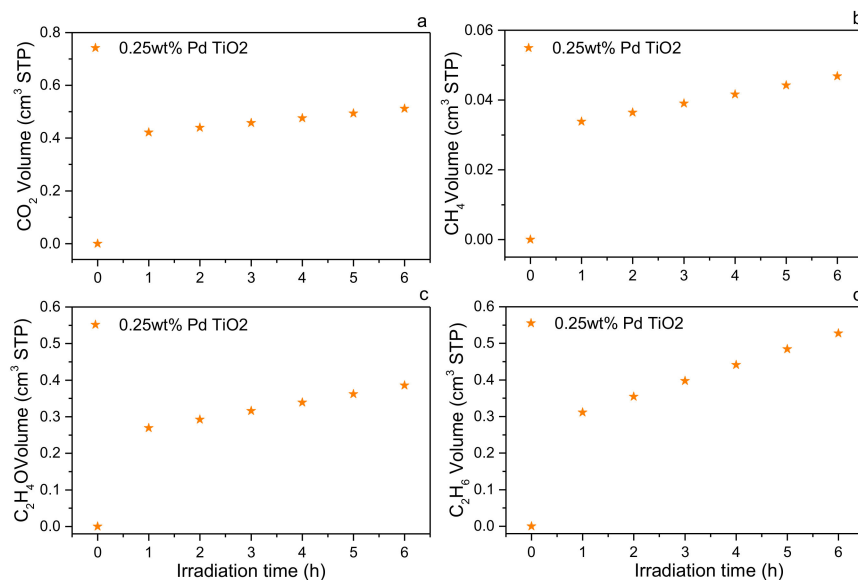


Figure 10. Hydrocarbon Profiles of (a) Carbon dioxide (CO₂), (b) Methane (CH₄), (c) Acetaldehyde (C₂H₄O) and (d) Ethane (C₂H₆) at 0.25 wt% Pd. Conditions: Photocatalyst concentration 0.15 g/L, 2.0 v/v% ethanol, argon atmosphere, pH = 4 ± 0.05 after UV light photoreduction.

2.4. Quantum Yield (QY) Evaluation

For the photoconversion of organic species, one can consider a Quantum Yield (QY) parameter. The QY calculation methodology is reported in Appendix D.

Effect of Pd Addition on Quantum Yields

The QY calculation for the TiO₂ photocatalysts calculation of the P_t transmitted photons, the P_i incident photons, and the P_{bs} backscattered photons, as described in Section 2.2.

Table 7 and Figure 11 report the QY% for the mesoporous photocatalysts doped with palladium at different metal loadings (0.25, 0.50, 1.00, 2.50, and 5.00 wt%) under the following conditions: (a) Photocatalyst slurry concentrations of 0.15 g/L, (b) 2.0 v/v% ethanol, (c) pH = 4 ± 0.05 and (d) Visible light.

Table 7. QYs% for Pd-TiO₂ Photocatalysts at Different Metal Loadings (0.25, 0.50, 1.00, 2.50, and 5.00 wt%) under: (a) Visible light irradiation only, (b) Using near-UV light followed by visible light irradiation.

Photocatalyst	QY (%) (a)	QY (%) (b)
TiO ₂	0.23	-
0.25 wt% Pd TiO ₂	1.13	1.58
0.50 wt% Pd TiO ₂	0.34	1.07
1.00 wt% Pd TiO ₂	0.30	0.80
2.50 wt% Pd TiO ₂	0.10	0.79
5.00 wt% Pd TiO ₂	0.10	0.78

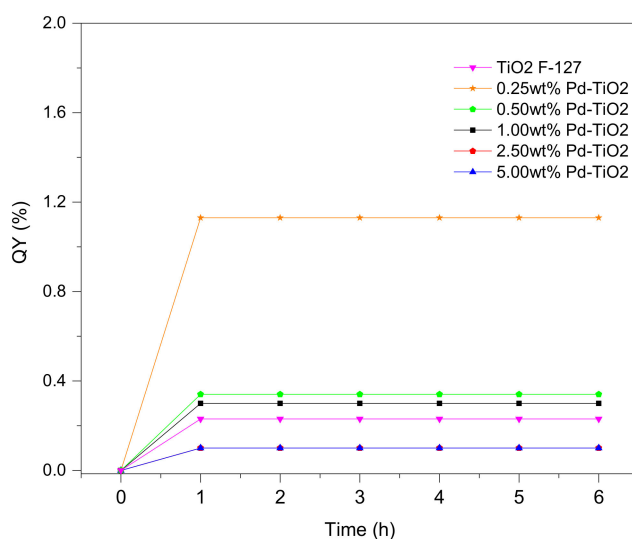


Figure 11. QY% at Various Irradiation Times under Visible Light using a 0.15 g/L of Photocatalyst Concentration. Note: Pd-TiO₂ photocatalyst with different palladium loadings: 0.25, 0.50, 1.00, 2.50, and 5.00 wt%.

One can observe in Table 6 that for all the prepared Pd-TiO₂ photocatalysts, the QYs% obtained while being irradiated with visible light were in the 0.10–1.13% low range. These low QYs% were assigned to the lack of ability of the Pd-TiO₂ photocatalysts to produce hydrogen under visible light with only 49.8 wt% of the loaded palladium as Pd°.

However, Table 6 also shows that when the photocatalysts were photoreduced with near-UV irradiation, the QYs% increased, reaching QY% values as high as 1.58%. These results demonstrate the importance of the noble metal photoreduction using near-UV irradiation (photoreduction). One should note that photoreduction was critical to making Pd-TiO₂ photocatalysts active under visible light for hydrogen production.

Few papers in the technical literature report QYs of a comparable magnitude. Some authors have used Pd-TiO₂ (0.3 wt%) and 3NbTi/Pt-Pd as photocatalysts, achieving maximum QYs between 0.43 and 1.2% [62–64]. As well, the absorbed photon rates were measured and calculated using a numerical solution of a radiation equation. These modeled absorption rates may involve significant errors. In this case, as stated before in the present study, the QYs% were determined by using an experimentally evaluated P_a , determined from MIEB macroscopic balances, as reported in Section 2.2.

Furthermore, Figure 12 reports the consistent QY% trends observed for Pd-doped TiO₂ photocatalysts as follows: (a) During the first hour of irradiation, the QY% increased progressively until they reached a stable value; and (b) During the six hours of irradiation that followed, the QY% remained unchanged, with the photocatalysts under study exhibiting a stable performance. It can also be observed that there is a significant increase of QY% when using 0.25 and 0.50 wt% Pd-TiO₂, whereas higher Pd loadings led to a decrease in the QY%.

It is also interesting to see in Figure 12, that the photoreduced semiconductors of the present study display good and stable QYs%, showing their significant ability to produce hydrogen. This photocatalyst stability was also established with 4 consecutive hydrogen production photocatalytic runs, each lasting 6 h or the equivalent of 24 h under visible light irradiation.

Based on the reported results, it is thus anticipated, that further research with mesoporous TiO₂ photocatalysts doped with noble metals will be valuable, particularly in the case of Pd-doped TiO₂ using ethanol as a scavenger. This will likely lead to stable and efficient photocatalytic processes for hydrogen production via water splitting. These Pd-TiO₂ photocatalysts may also present significant cost advantages versus other noble metal dopants such as Ta, Nb or Pt.

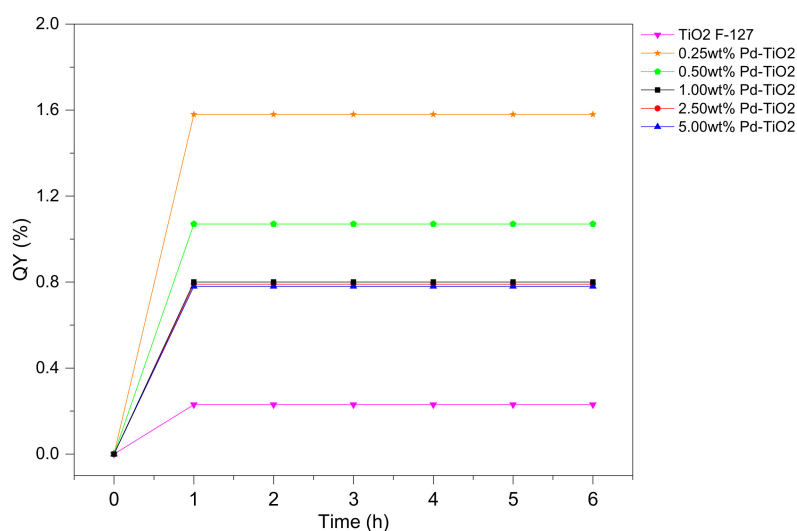


Figure 12. QY% at Various Irradiation Times, under Visible Light, using a 0.15 g/L of Photocatalyst Concentration. Notes: (a) Pd on TiO₂ photocatalyst with palladium loadings: 0.25, 0.5, 1.0, 2.5 and 5.0 wt%) and (b) Photocatalysts photoreduced using Near-UV irradiation for 1 h.

3. Experimental Methods

The photocatalyst of the present study was synthesized using a sol-gel methodology [53]. Different techniques were utilized for its characterization as follows: (a) Specific Surface Area (BET), (b) Chemisorption, (c) X-ray Diffraction, (d) TPR Analysis, (e) XPS and (f) UV-Vis Absorption. These techniques allowed the determination of the surface area, the pore size distribution and the pore size, the phase composition, the band gap, the metal dispersion, the temperature-programmed reduction and the Pd⁰ crystallite size of the photocatalyst.

3.1. Photocatalyst Synthesis

The synthesis of the photocatalyst of the present study via the sol-gel method requires the following: (a) ethanol USP (C₂H₅OH) obtained from commercial alcohols, (b) hydrochloric acid (HCl, 37% purity), (c) pluronic F-127, (d) anhydrous citric acid, (e) titanium (IV) isopropoxide, and (f) palladium (II) chloride (PdCl₂, 99.9% purity). All the reagents were purchased from Sigma Aldrich (Oakville, Ontario, Canada). Detailed information about the photocatalyst synthesis methodology is reported in Appendix B.

According to the methodology proposed by Das et al. [65], 20 mL ethanol was acidified with 1.65 g of hydrochloric acid. This was followed by the addition of 1 g of copolymer pluronic F-127. The mixture was stirred for 30 min until complete dissolution was reached. 0.315 g of anhydrous citric acid was mixed with 1 mL of water and added to the initial solution. The resultant mixture was stirred for 2 h. Following this, 1.42 g of titanium IV isopropoxide in ethanol added dropwise [29].

Furthermore, and after this, PdCl₂ was added to the resulting sol-gel suspension, given its solubility under the conditions of the sol-gel suspension. PdCl₂ was incorporated at different concentrations to achieve 0.25–5.00 wt% Pd loadings. The resulting sol-gel suspension was stirred for 24–48 h and then calcined under an air atmosphere at 500 °C for 6 h [66]. This allowed the copolymer to be removed, with an ordered mesoporous titanium framework being formed [67,68].

However, and considering that palladium oxidizes during the calcination step, the resulting photocatalyst had to be reduced in a subsequent step. To accomplish this, the synthesized semiconductor was placed in a flow reactor unit under an atmosphere of 1 cm³/s of Ar/H₂ (g) (90/10%, Praxair) at 500 °C for 3 h [69]. Given that this reduction with hydrogen was incomplete, a further and critical Pd-TiO₂ photoreduction step was implemented in the Photo-CREC Water-II (PCW-II), by exposing the photocatalyst to near-UV light at room temperature for 60 min.

3.2. Equipment

The Photo-CREC Water-II (PCW-II) Reactor is an innovative unit for hydrogen production. It is a slurry batch reactor with a total volume of 6 L. As seen in Figure 13, it is composed of: (1) A 15-W fluorescent visible light lamp, (2) A Pyrex glass inner tube where the lamp is placed, (3) A black polyethylene outer tube, (4) A centrifugal pump, (5) Two sampling ports where the photocatalyst suspension is always kept sealed under agitation, one for the liquid phase and the other one for the gas phase, (6) A hydrogen storage tank, and (7) Silica windows for irradiation measurements [70]. Refer to Appendix C for a detailed lamp characterization.

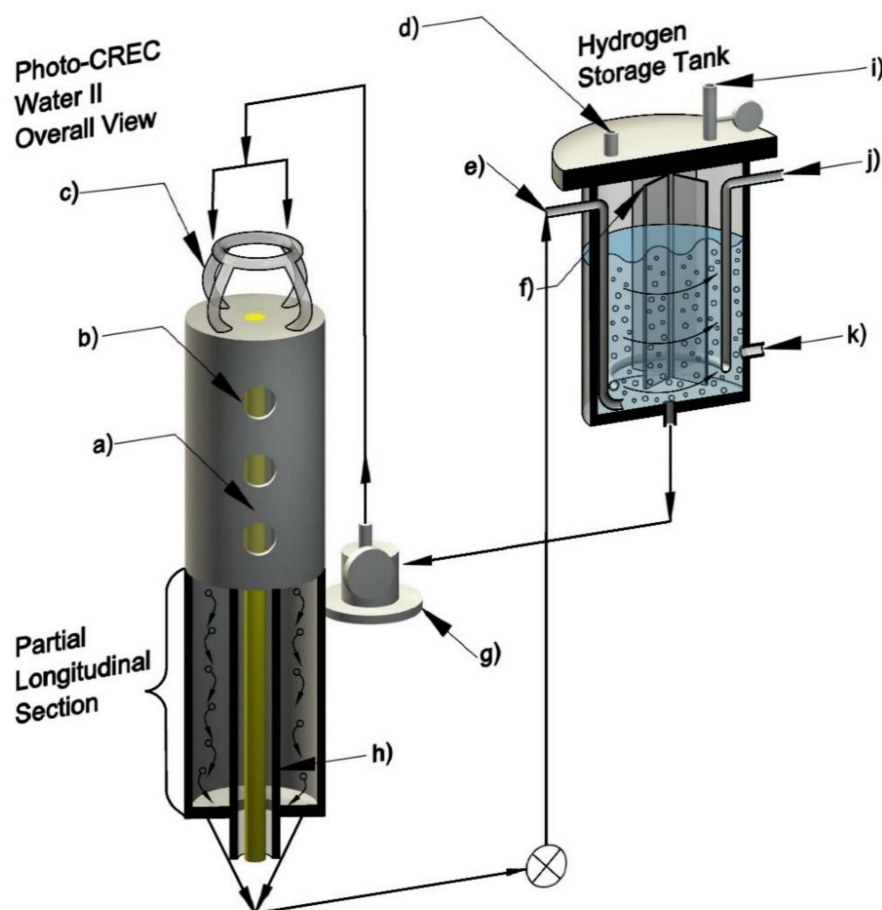


Figure 13. Schematics of the Photo-CREC Water II Reactor. Components: (a) Opaque polyethylene tube, (b) Fused silica windows, (c) Flow distributor, (d) Gas sampling port, (e) Jet driving mixing port, (f) Self-driven mixing impeller, (g) Centrifugal pump, (h) Pyrex tube, (i) Draining gas valve, (j) Purging gas injector, and (k) Slurry sampling port.

3.3. Photocatalyst Characterization

Nitrogen adsorption and desorption isotherms at $-195\text{ }^{\circ}\text{C}$ were measured using a Micromeritics ASAP 2010 Surface Area and Porosity analyzer (Norcross, GA, U.S.A). The samples were initially degassed in a vacuum at $300\text{ }^{\circ}\text{C}$ for 3 h. The BET-surface area was determined from the BET plot. The pore volume was measured at a relative pressure of $P/P_0 = 0.99$. To estimate the pore size distribution, the N_2 physisorption BJH (Barrett–Joyner–Halenda) method was used [71].

Pulse chemisorption with the Micromeritics AutoChem II Analyzer (Norcross, GA U.S.A) was utilized to determine the fraction of dispersed metal. On the other hand, the XRD spectrum for each material was measured in a Rigaku Rotating Anode X-ray Diffractometer (Rigaku, Auburn Hills, MI, United States) rated at 45 kV and 160 mA, to identify the crystalline phases of the materials.

The diffractograms were taken in the 2θ angle scale (20° – 80° range), with a step size of 0.02° and a dwell time of 2 s/step.

The H_2 Temperature Programmed Reduction (TPR) analyses of the Pd-TiO₂ photocatalysts were evaluated in a Micromeritics AutoChemII Analyzer. 250 mg of the photocatalyst were placed in the U-tube with a gas reduction mixture of Ar/H₂ (g) (90/10%). The reaction temperature was kept within a 0° to 600° C range with a flow rate of 50 mL min^{-1} . The amount of H₂ consumed during the reduction was measured by a thermal conductivity detector (TCD) [42].

To determine the band gap, a UV-VIS-NIR Spectrophotometer (Shimadzu UV-3600, Nakagyo-ku, Kyoto, Japan) was used, with the BaSO₄ as a reference [48]. By using the Kubelka–Munk (K–M) methodology, Tauc plots were developed, in order to establish the corresponding band gaps for each photocatalyst [72]. Furthermore, to ascertain the composition and the oxidation/reduction state of palladium, an X-ray Photoelectron Spectroscopy (XPS) analysis was utilized [73].

Furthermore, to measure the irradiation of the visible light lamp inside the Photo-CREC Water-II, the Stellar Net EPP2000-25 Spectrometer (StellarNet Inc., StellarNet, Inc., Tampa, Florida, U.S.A.) was used. The light source used was a fluorescent mercury Philips lamp (15 W) with an output power of 1.48 W and an average emitted photon energy of 274.5 kJ/photon mole.

3.4. Hydrogen Production

The Photo-CREC Water-II Reactor was used to evaluate the Pd-TiO₂ photocatalyst utilized during the water splitting runs. 6000 mL runs of water were used as the main reagent. As well, ethanol served as an organic scavenger. The pH was set to 4 ± 0.05 with H₂SO₄ [2M]. A BLB UV lamp was turned on for 60 min to photoreduce the PdO present in the semiconductor. After the first hour, the UV lamp was replaced by the Phillips Visible light lamp to initiate the reaction. Then, the water splitting run continued during (6) hours of irradiation [69].

The photocatalyst was loaded at a concentration of 0.15 g/L and sonicated for 10 min to avoid particle agglomeration. This ensured a homogeneous distribution of the photocatalyst throughout the reactor. To avoid any undesirable oxidation reaction, an argon flow was circulated for 10 min to keep an inert atmosphere.

The gases produced were evaluated by making use of a Shimadzu GC2010 Gas Chromatograph (Nakagyo-ku, Kyoto, Japan), which took consecutive gas samples every hour for 6 h. Argon (Praxair 99.999%) was used as a gas carrier. The GC possessed 2 detectors: a Flame Ionization Detector (Nakagyo-ku, Kyoto, Japan) (FID) and a Thermal Conductivity Detector (TCD). This unit also included a HayeSepD 100/120 mesh packed column ($9.1\text{ m} \times 2\text{ mm} \times 2\text{ }\mu\text{m}$ nominal SS) (Kenilworth, NJ, U.S.A.). This equipment is capable of detecting hydrogen (H₂), carbon monoxide (CO), carbon dioxide (CO₂), and methane (CH₄) among other hydrocarbon organic species.

4. Conclusions

Palladium-doped TiO₂ photocatalysts, photoreduced with near-UV irradiation prior to their utilization, are shown to favor hydrogen production under visible light. The structural properties of the best performing photocatalysts (0.25 wt%Pd-TiO₂) were established using X-ray Diffraction (XRD), BET Surface Area (S_{BET}), Temperature Programmed Reduction (TPR), Chemisorption and X-ray Photoelectron Spectroscopy (XPS), and UV-Vis Reflectance Spectroscopy. It was shown that the near-UV photoreduced 0.25 wt%Pd-TiO₂ enhances hydrogen formation, reaching in 6 h, 8.0 cm^3 STP of produced hydrogen. The 0.25 wt% Pd on TiO₂ also displays in all cases, a zero-order kinetics, with a highest QY% of 1.58%. These positive findings set favorable prospects for further research, including the development of a kinetic model which's availability is considered critical for the scaling up of a Photo-CREC-Water II unit for hydrogen production.

Author Contributions: Conceptualization, investigation and supervision, H.d.L.; Proposed methodology and supervision, S.E.; Validation, formal analysis and writing, B.R. All authors have read and agreed to the published version of the manuscript.

Funding: This research was funded by the Natural Sciences and Engineering Research Council of Canada (NSERC) and the University of Western Ontario, through grants awarded to Hugo de Lasa.

Acknowledgments: We would like to gratefully thank Florencia de Lasa who assisted with the editing of this paper and the drafting of the graphical abstract of the present article.

Conflicts of Interest: The authors declare no conflict of interest.

Nomenclature

CO ₂	Carbon dioxide
CH ₄	Methane
C ₂ H ₆	Ethane
C ₂ H ₄ O	Acetaldehyde
c	Speed of light (3.0×10^8 m/s)
D _p	Pore diameter (cm)
e ⁻	Electron
h ⁺	Hole
h	Planck's constant (6.63×10^{-34} J/s)
E _{bg}	Energy band gap (eV)
E _{av}	Average energy of a photon (kJ/mol photon)
F-127	Poly (ethylene oxide)/poly (propylene oxide)/poly (ethylene oxide)
H•	Hydrogen radical
H ₂ O	Water
I(λ)	Intensity of light (W/cm ²)
OH ⁻	Hydroxide ions
OH•	Hydroxide radicals
P-123	Poly (ethylene glycol)-block-poly (propylene glycol)-block-poly (ethylene glycol)
P ₀	Rate of photons emitted by the BLB lamp (einstein/s)
P _a	Rate of absorbed photons (einstein/s)
P _{a-wall}	Rate of photons absorbed by the inner pyrex glass (einstein/s)
P _{bs}	Rate of backscattered photons exiting the system (einstein/s)
Pd	Palladium
PdCl ₂	Palladium II chloride
PEO	Poly (ethylene oxide)
P _{fs}	Rate of forward-scattered radiation (einstein/s)
P _i	Rate of photons reaching the reactor inner surface (einstein/s)
P _{ns}	Rate of transmitted non-scattered radiation (einstein/s)
PPO	Poly (propylene oxide)
Pt	Rate of transmitted photons (einstein/s)
Pt	Platinum
q (θ, z, λ, t)	Net radiative flux over the lamp emission spectrum (μW/cm ²)
t	Time (h)
TiO ₂	Titanium dioxide
V	Total volume of the gas chamber (5716 cm ³)
VP	pore volume
W	Weight (g)
Wt%	Weight percent (% m/m)

Greek symbols

θ	Diffraction angle, also scattering angular angle (o)
λ	Wave length (nm)
φ	Quantum Yield Efficiency (%)

Acronyms

Bg	Band Gap
BJH	Barrett–Joyner–Halenda Model
BLB	Black Light Blue Lamp
BET	Brunauer–Emmett–Teller Surface Area Method
CB	Conduction Band
DP25	Degussa P25 (TiO ₂)
EISA	Evaporation-Induced-Self-Assembly
FID	Flame Ionization Detector
JCPDS	International Centre for Diffraction Data
K-M	Kubelka-Munk
MIEB	Macroscopic Irradiation Energy Balance
PCW-II	Photo-CREC Water II Reactor
PC	Photocatalyst Concentration
STP	Standard Temperature and Pressure (273 K and 1 atm)
TPR	Temperature Programmed Reduction
TCD	Thermal Conductivity Detector
UV	Ultraviolet
VB	Valence Band
XPS	X-ray Photoelectron Spectroscopy
XRD	X-ray Diffraction

Appendix A. Macroscopic Irradiation Energy Balance (MIEB)

The various terms in Equation (1) can be calculated as follows:

- (a) P_i is the rate of photons reaching the slurry suspension:

$$P_i = P_0 - P_{a-wall} \text{ (Einstein/s)} \quad (\text{A1})$$

with P_0 , the rate of photons emitted by the lamp being estimated from radiometric measurements; where $q(\theta, z, \lambda)$ is the radiative flux expressed in $\text{J s}^{-1} \text{m}^{-3}$, where λ is the photon wavelength expressed in nm, where r represents the radial coordinate expressed in m, where z stands for the axial coordinate expressed in m, where h represents the Planck's constant expressed in J s , and where c denotes the speed of light expressed in m s^{-1} .

$$P_0 = \int_{\lambda_1}^{\lambda_2} \lambda \int_0^L \int_0^{2\pi} q(\theta, Z, \lambda) r d\theta dz d\lambda \quad (\text{A2})$$

And P_{a-wall} is the rate of photons absorbed by the inner Pyrex glass surface.

- (b) P_{bs} represents the difference between P_i and $P_{t|c \rightarrow 0+}$. It is the rate of photons transmitted at a photocatalyst concentration approaching zero [28] as follows:

$$P_{bs} = P_i - P_{t|c \rightarrow 0+} \quad (\text{A3})$$

- (c) P_t accounts for the difference between the transmitted non-scattered radiation (P_{ns}) and the forward-scattered radiation (P_{fs}):

$$P_t = P_{ns} - P_{fs} \quad (\text{A4})$$

The described macroscopic balances were originally developed for near-UV irradiation in photocatalytic reactors [70]. However, given that these macroscopic balances are not photon wavelength dependant, they were extended to visible light irradiation.

Appendix B. Photocatalyst Synthesis—EISA Method

In this research, the photocatalyst synthesis uses the Evaporation-Induced-Self-Assembly (EISA) Method. This approach has been utilized in the preparation of semiconductors when adding a template to control the material pore size [74]. This methodology was applied in the present study, given that: (a) It is easy to use, (b) it allows close control of the pore size distribution with the selected copolymer template, (c) it enhances the specific surface area, (d) It is relatively inexpensive, and (e) it does not require special equipment [75]. Figure A1 describes the photocatalyst synthesis based on a sol-gel method with the use of a polymeric template [pluronic F-127 (PEO₁₀₆PPO₇₀PEO₁₀₆)], a metallic precursor [titanium IV isopropoxide] and an active metal [PdCl₂] precursor. The mixing of these components leads to the formation of micelles and subsequently to a mesoporous structure. Subsequent calcination and reduction yield: (a) An adequate template removal, and (b) The formation of mesopores with highly dispersed palladium nanoparticles [76].

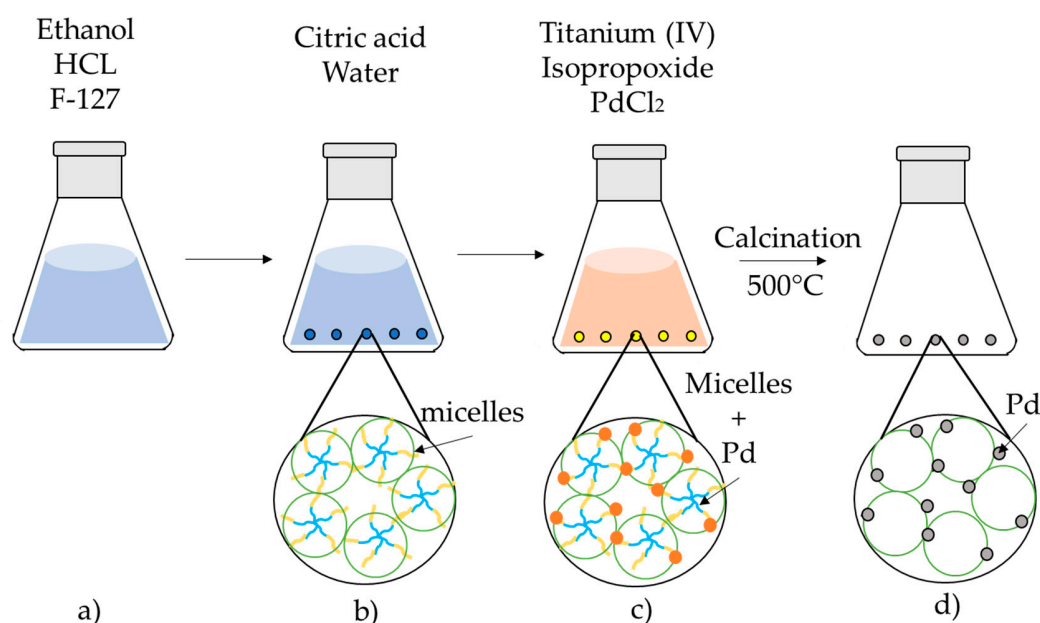


Figure A1. Description of the Four Consecutive Steps during Pd-Doped TiO₂ Photocatalyst Preparation: (a) Ethanol enters the interface between the hydrophilic (PEO) and hydrophobic (PPO) chains and attaches to the hydrophobic core, (b) A hydrophobic block (PPO) is placed in a central location surrounded by the PEO tails forming micelles, (c) The PEO tails become attached to the TiO₂, leaving a hybrid outer layer with a dominant TiO₂ composition, and (d) Calcination of the resulting photocatalyst precursor yields TiO₂ with a 3D mesoporous structure [57].

Appendix C. Lamp Characterization

Figure A2 reports the spectrum of the polychromatic BLB Ushio near-UV lamp, with an observed output power of 1.61 W and a 325.1 kJ/mole of photons average.

Figure A3 reports the spectrum of the mercury Philips visible light lamp. It has an output power of 1.48 W and an average emitted photon energy of 274.5 kJ/photon mole.

The axial distribution of the radiative flux was determined using the Stellar Ney EPP2000-25 Spectrometer. Figure A4 displays the observed axial visible lamp radiation distribution with the radiation significantly decreasing, in the lower and upper axial lamp positions [77].

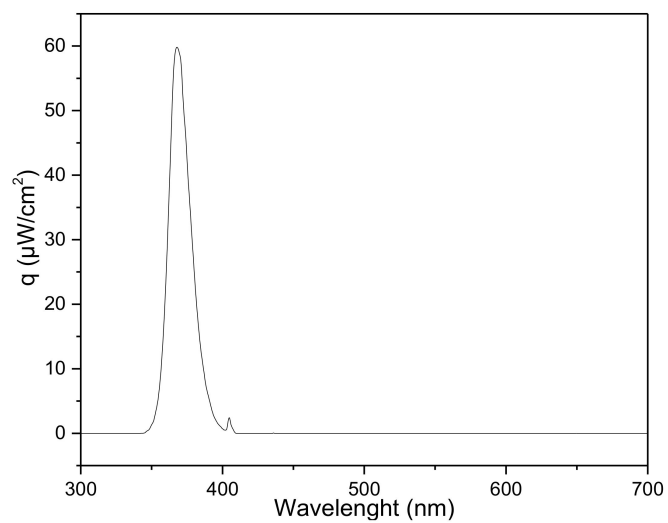


Figure A2. Near-UV Lamp Irradiation Spectrum.

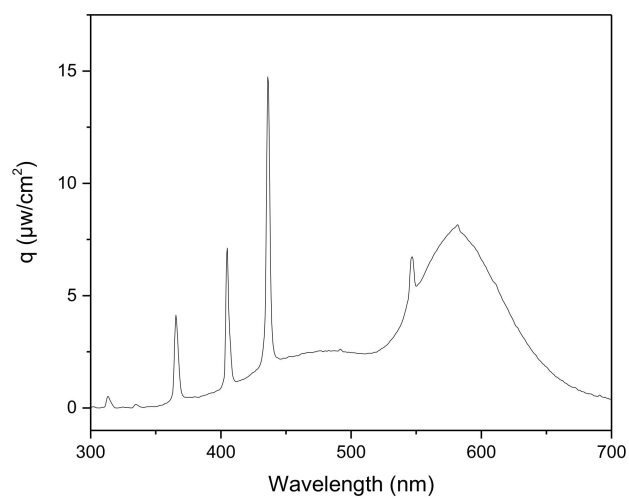


Figure A3. Visible Lamp Irradiation Spectrum.

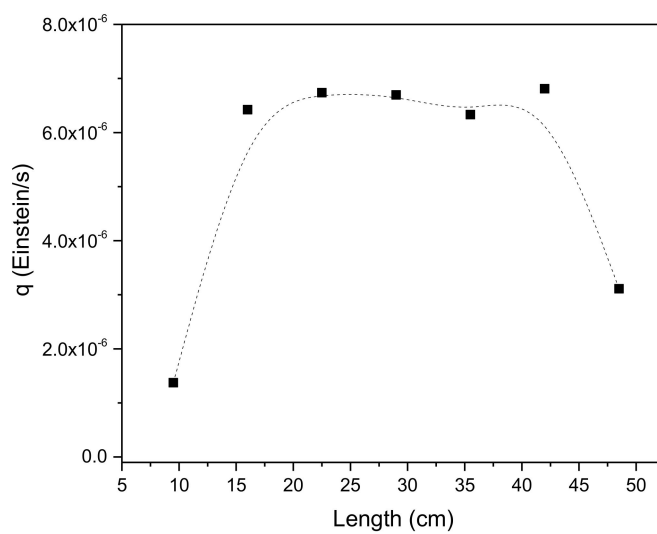


Figure A4. Visible Lamp Axial Distribution.

Appendix D. Quantum Yield Calculation

The QY is defined as the formed H \cdot molar rate over the absorbed photons molar rate. Thus, it describes the extent of the photochemical utilization for hydrogen production of absorbed photons [34]. The QY is calculated according to the following equation:

$$QY_{H\cdot} = \frac{\text{moles of } H\cdot / s}{\text{moles of photons absorbed by the photocatalyst} / s} \quad (\text{A5})$$

Equation (A4) is equal to:

$$\%QY = \frac{\left[\frac{dN_{H\cdot}}{dt} \right]}{P_a} \times 100 \quad (\text{A6})$$

where, $\frac{dN_{H\cdot}}{dt}$ is the rate of moles of hydrogen radicals formed at any time during the photocatalyst irradiation.

To calculate the QY, the P_a or the moles of absorbed photons is needed. The P_a was determined by using the MIEB in the Photo-CREC Water-II Reactor [69], as described in Section 2.2.

References

- Chiarello, G.L.; Dozzi, M.V.; Selli, E. TiO₂-based materials for photocatalytic hydrogen production. *J. Energy Chem.* **2017**, *26*, 250–258. [CrossRef]
- Higashi, M.; Domen, K.; Abe, R. Highly Stable Water Splitting on Oxynitride TaON Photoanode System under Visible Light Irradiation. *J. Am. Chem. Soc.* **2012**, *134*, 6968–6971. [CrossRef] [PubMed]
- Ishikawa, A.; Takata, T.; Kondo, J.N.; Hara, M.; Kobayashi, H.; Domen, K. Oxysulfide Sm₂Ti₂S₂O₅ as a Stable Photocatalyst for Water Oxidation and Reduction under Visible Light Irradiation ($\lambda \leq 650$ nm). *J. Am. Chem. Soc.* **2002**, *124*, 13547–13553. [CrossRef] [PubMed]
- Wang, D.; Pierre, A.; Kibria, M.G.; Cui, K.; Han, X.; Bevan, K.H.; Guo, H.; Paradis, S.; Hakima, A.-R.; Mi, Z. Wafer-Level Photocatalytic Water Splitting on GaN Nanowire Arrays Grown by Molecular Beam Epitaxy. *Nano Lett.* **2011**, *11*, 2353–2357. [CrossRef]
- Abe, R.; Sayama, K.; Sugihara, H. Development of New Photocatalytic Water Splitting into H₂ and O₂ using Two Different Semiconductor Photocatalysts and a Shuttle Redox Mediator IO₃⁻/I⁻. *J. Phys. Chem. B* **2005**, *109*, 16052–16061. [CrossRef]
- Zou, Z.; Ye, J.; Sayama, K.; Arakawa, H. Direct splitting of water under visible light irradiation with an oxide semiconductor photocatalyst. *Nature* **2001**, *414*, 625–627. [CrossRef]
- Zuo, F.; Wang, L.; Wu, T.; Zhang, Z.; Borchardt, D.; Feng, P. Self-Doped Ti³⁺ Enhanced Photocatalyst for Hydrogen Production under Visible Light. *J. Am. Chem. Soc.* **2010**, *132*, 11856–11857. [CrossRef]
- Jensen, S.H.; Larsen, P.H.; Mogensen, M. Hydrogen and synthetic fuel production from renewable energy sources. *Int. J. Hydrogen Energy* **2007**, *32*, 3253–3257. [CrossRef]
- Mazloomi, K.; Gomes, C. Hydrogen as an energy carrier: Prospects and challenges. *Renew. Sustain. Energy Rev.* **2012**, *16*, 3024–3033. [CrossRef]
- Ipsakis, D.; Voutetakis, S.; Seferlis, P.; Stergiopoulos, F.; Elmasides, C. Power management strategies for a stand-alone power system using renewable energy sources and hydrogen storage. *Int. J. Hydrogen Energy* **2009**, *34*, 7081–7095. [CrossRef]
- Dozzi, M.V.; Selli, E. Doping TiO₂ with p-block elements: Effects on photocatalytic activity. *J. Photochem. Photobiol. C Photochem. Rev.* **2013**, *14*, 13–28. [CrossRef]
- Liu, G.; Wang, L.; Yang, H.G.; Cheng, H.-M.; Lu, G.Q.M. Titania-based photocatalysts—Crystal growth, doping and heterostructuring. *J. Mater. Chem.* **2010**, *20*, 831–843. [CrossRef]
- Mills, A. An overview of semiconductor photocatalysis. *J. Photochem. Photobiol. A Chem.* **1997**, *108*, 1–35. [CrossRef]
- Abe, R. Significant effect of iodide addition on water splitting into H₂ and O₂ over Pt-loaded TiO₂ photocatalyst: Suppression of backward reaction. *Chem. Phys. Lett.* **2003**, *371*, 360–364. [CrossRef]
- Mills, A. Photosensitised dissociation of water using dispersed suspensions of n-type semiconductors. *J. Chem. Soc. Faraday Trans. 1 Phys. Chem. Condens. Phases* **1982**, *12*, 3659–3669. [CrossRef]

16. López, C.R.; Melián, E.P.; Ortega Méndez, J.A.; Santiago, D.E.; Rodríguez, J.M.; González Díaz, O. Comparative study of alcohols as sacrificial agents in H₂ production by heterogeneous photocatalysis using Pt/TiO₂ catalysts. *J. Photochem. Photobiol. A Chem.* **2015**, *312*, 45–54. [[CrossRef](#)]
17. Galińska, A. Photocatalytic Water Splitting over Pt–TiO₂ in the Presence of Sacrificial Reagents. *Energy Fuels* **2005**, *19*, 1143–1147. [[CrossRef](#)]
18. Chen, X.; Shen, S.; Guo, L.; Mao, S.S. Semiconductor-based photocatalytic hydrogen generation. *Chem. Rev.* **2010**, *110*, 6503–6570. [[CrossRef](#)]
19. Acar, C. Review of photocatalytic water-splitting methods for sustainable hydrogen production. *Energy Res.* **2016**, *40*, 1449–1473. [[CrossRef](#)]
20. Cushing, S.K.; Li, J.; Meng, F.; Senty, T.R.; Suri, S.; Zhi, M.; Li, M.; Bristow, A.D.; Wu, N. Photocatalytic activity enhanced by plasmonic resonant energy transfer from metal to semiconductor. *J. Am. Chem. Soc.* **2012**, *134*, 15033–15041. [[CrossRef](#)]
21. Melián, E.P.; López, C.R.; Méndez, A.O.; Díaz, O.G.; Suárez, M.N.; Rodríguez, J.M.D.; Navío, J.A.; Hevia, D.F. Hydrogen production using Pt-loaded TiO₂ photocatalysts. *Int. J. Hydrogen Energy* **2013**, *38*, 11737–11748. [[CrossRef](#)]
22. Olivo, A.; Ghedini, E.; Signoretto, M.; Compagnoni, M.; Rossetti, I. Liquid vs. Gas Phase CO₂ Photoreduction Process: Which Is the Effect of the Reaction Medium? *Energies* **2017**, *10*, 1394. [[CrossRef](#)]
23. Castro, A.L. Synthesis of anatase TiO₂ nanoparticles with high temperature stability and photocatalytic activity. *Solid State Sci.* **2008**, *10*, 602–606. [[CrossRef](#)]
24. Holloway, P.; McGuire, G. *Handbook of Compound Semiconductor*; Noyes Publications: Park Ridge, NJ, USA, 1995.
25. Ahmad, H.; Kamarudin, S.K.; Minggu, L.J.; Kassim, M. Hydrogen from photo-catalytic water splitting process: A review. *Renew. Sustain. Energy Rev.* **2015**, *43*, 599–610. [[CrossRef](#)]
26. Yang, J. Roles of Cocatalysts in Photocatalysis and Photoelectrocatalysis. *Acc. Chem. Res.* **2013**, *46*, 1900–1909. [[CrossRef](#)]
27. Hou, L.; Zhang, M.; Guan, Z.; Li, Q.; Yang, J. Effect of platinum dispersion on photocatalytic performance of Pt–TiO₂. *J. Nanopart. Res.* **2018**, *20*, 60. [[CrossRef](#)]
28. Escobedo, S.; Serrano, B.; Calzada, A.; Moreira, J.; De Lasa, H. Hydrogen production using a platinum modified TiO₂ photocatalyst and an organic scavenger. Kinetic modeling. *Fuel* **2016**, *181*, 438–449. [[CrossRef](#)]
29. Guayaquil-Sosa, J.F.; Serrano-Rosales, B.; Valadés-Pelayo, P.J.; de Lasa, H. Photocatalytic hydrogen production using mesoporous TiO₂ doped with Pt. *Appl. Catal. B Environ.* **2017**, *211*, 337–348. [[CrossRef](#)]
30. Etacheri, V.; di Valentin, C.; Schneider, J.; Bahnemann, D.; Pillai, S.C. Visible-light activation of TiO₂ photocatalysts: Advances in theory and experiments. *J. Photochem. Photobiol. C Photochem. Rev.* **2015**, *25*, 1–29. [[CrossRef](#)]
31. Abdelaal, M.Y.; Mohamed, R.M. Novel Pd/TiO₂ nanocomposite prepared by modified sol–gel method for photocatalytic degradation of methylene blue dye under visible light irradiation. *J. Alloys Compd.* **2013**, *576*, 201–207. [[CrossRef](#)]
32. Espino-Estévez, M.R.; Fernández-Rodríguez, C.; González-Díaz, O.M.; Araña, J.; Espinós, J.P.; Ortega-Méndez, J.A.; Doña-Rodríguez, J.M. Effect of TiO₂–Pd and TiO₂–Ag on the photocatalytic oxidation of diclofenac, isoproturon and phenol. *Chem. Eng. J.* **2016**, *298*, 82–95. [[CrossRef](#)]
33. Wahyuni, E.T.; Kuncaka, A.; Sutarno, S. Application of Photocatalytic Reduction Method with TiO₂ for Gold Recovery. *Chemistry* **2015**, *3*, 207–211.
34. Lasa, H.D.; Rosales, B.S.; Moreira, J.; Valades-Pelayo, P. Efficiency Factors in Photocatalytic Reactors: Quantum Yield and Photochemical Thermodynamic Efficiency Factor. *Chem. Eng. Technol.* **2016**, *39*, 51–65. [[CrossRef](#)]
35. Endang, H.A.; Nurul, T.W. Photoreduction Processes over TiO₂ Photocatalyst. In *Photocatalysts—Applications and Attributes*; IntechOpen: London, UK, 2018; p. 17.
36. Pan, X.; Xu, Y.J. Defect-mediated growth of noble-metal (Ag, Pt, and Pd) nanoparticles on TiO₂ with oxygen vacancies for photocatalytic redox reactions under visible light. *J. Phys. Chem. C* **2013**, *117*, 17996–18005. [[CrossRef](#)]
37. AutoChem 2920 Automated Catalyst Characterization System. In *Operator's Manual*; Micromeritics Instrument Corporation: Norcross, GA, USA, 2014.

38. Treacy, J.P.W.; Hussain, H.; Torrelles, X.; Grinter, D.; Cabailh, G.; Bikondoa, O.; Nicklin, C.; Selcuk, S.; Selloni, A.; Lindsay, R.; et al. Geometric structure of anatase TiO₂(101). *Phys. Rev. B* **2017**, *95*, 1–7. [[CrossRef](#)]
39. Deshmane, V.G.; Owen, S.L.; Abrokwah, R.Y.; Kuila, D. Mesoporous nanocrystalline TiO₂ supported metal (Cu, Co, Ni, Pd, Zn, and Sn) catalysts: Effect of metal-support interactions on steam reforming of methanol. *J. Mol. Catal. A Chem.* **2015**, *408*, 202–213. [[CrossRef](#)]
40. Mendez, C.M.; Olivero, H.; Damiani, D.E.; Volpe, M.A. On the role of Pd β-hydride in the reduction of nitrate over Pd based catalyst. *Appl. Catal. B Environ.* **2008**, *84*, 156–161. [[CrossRef](#)]
41. Baylet, A.; Marécot, P.; Duprez, D.; Castellazzi, P.; Groppi, G.; Forzatti, P. In situ Raman and in situ XRD analysis of PdO reduction and Pd⁰ oxidation supported on γ-Al₂O₃ catalyst under different atmospheres. *Phys. Chem. Chem. Phys.* **2011**, *13*, 4607. [[CrossRef](#)]
42. Bratan, V.; Munteanu, C.; Hornoiu, C.; Vasile, A.; Papa, F.; State, R.; Preda, S.; Culita, D.; Ionescu, N.I. CO oxidation over Pd supported catalysts—In situ study of the electric and catalytic properties. *Appl. Catal. B Environ.* **2017**, *207*, 166–173. [[CrossRef](#)]
43. González, C.A.; Ardila, A.N.; de Correa, C.M.; Martínez, M.A.; Fuentes-Zurita, G. Pd/TiO₂ Washcoated Cordierite Minimonoliths for Hydrodechlorination of Light Organochlorinated Compounds. *Ind. Eng. Chem. Res.* **2007**, *46*, 7961–7969. [[CrossRef](#)]
44. Tauc, A.; Grigorovici, J.; Vancu, R. Optical Properties and Electronic Structure of Amorphous Germanium. *Basic Solid State Phys.* **1966**, *15*, 627–637. [[CrossRef](#)]
45. Santara, B.; Pal, B.; Giri, P.K. Signature of strong ferromagnetism and optical properties of Co doped TiO₂ nanoparticles. *J. Appl. Phys.* **2011**, *110*, 114322. [[CrossRef](#)]
46. Khairy, W.; Zakaria, M. Effect of metal-doping of TiO₂ nanoparticles on their photocatalytic activities toward removal of organic dyes. *Egypt. J. Pet.* **2014**, *23*, 419–426. [[CrossRef](#)]
47. Ola, O.; Maroto-Valer, M.M. Transition metal oxide based TiO₂ nanoparticles for visible light induced CO₂ photoreduction. *Appl. Catal. A Gen.* **2015**, *502*, 114–121. [[CrossRef](#)]
48. Sobana, N.; Muruganadham, M.; Swaminathan, M. Nano-Ag particles doped TiO₂ for efficient photodegradation of Direct azo dyes. *J. Mol. Catal. A Chem.* **2006**, *258*, 124–132. [[CrossRef](#)]
49. Leong, K.H.; Chu, H.Y.; Ibrahim, S.; Saravanan, P. Palladium nanoparticles anchored to anatase TiO₂ for enhanced surface plasmon resonance-stimulated, visible-light-driven photocatalytic activity. *Beilstein J. Nanotechnol.* **2015**, *6*, 428–437. [[CrossRef](#)]
50. Yang, X.; Ma, F.; Li, K.; Guo, Y.; Hu, J.; Li, W.; Huo, M.; Guo, Y. Mixed phase titania nanocomposite codoped with metallic silver and vanadium oxide: New efficient photocatalyst for dye degradation. *J. Hazard. Mater.* **2010**, *175*, 429–438. [[CrossRef](#)]
51. Kuvarega, A.T.; Krause, R.W.M.; Mamba, B.B. Nitrogen / Palladium-Codoped TiO₂ for Efficient Visible Light Photocatalytic Dye Degradation. *J. Phys. Chem. C* **2011**, *115*, 22110–22120. [[CrossRef](#)]
52. Lee, Y.; Kim, E.; Park, Y.; Kim, J.; Ryu, W.H.; Rho, J.; Kim, K. Photodeposited metal-semiconductor nanocomposites and their applications. *J. Mater.* **2018**, *4*, 83–94. [[CrossRef](#)]
53. Peng, J.; Wang, S. Performance and characterization of supported metal catalysts for complete oxidation of formaldehyde at low temperatures. *Appl. Catal. B Environ.* **2007**, *73*, 282–291. [[CrossRef](#)]
54. Gomes, J.F.; Leal, I.; Bednarczyk, K.; Gmurek, M.; Stelmachowski, M.; Diak, M.; Emilia Quinta-Ferreira, M.; Costa, R.; Quinta-Ferreira, R.M.; Martins, R.C. Photocatalytic ozonation using doped TiO₂ catalysts for the removal of parabens in water. *Sci. Total Environ.* **2017**, *609*, 329–340. [[CrossRef](#)] [[PubMed](#)]
55. Maicu, M.; Hidalgo, M.C.; Colón, G.; Navío, J.A. Comparative study of the photodeposition of Pt, Au and Pd on pre-sulphated TiO₂ for the photocatalytic decomposition of phenol. *J. Photochem. Photobiol. A Chem.* **2011**, *217*, 275–283. [[CrossRef](#)]
56. Bahruji, H.; Bowker, M.; Davies, P.R.; Morgan, D.J.; Morton, C.A.; Egerton, T.A.; Kennedy, J.; Jones, W. Rutile TiO₂-Pd Photocatalysts for Hydrogen Gas Production from Methanol Reforming. *Top. Catal.* **2015**, *58*, 70–76. [[CrossRef](#)]
57. Rusinque, B.; Escobedo, S.; de Lasa, H. Photocatalytic hydrogen production under near-UV using Pd-doped mesoporous TiO₂ and ethanol as organic scavenger. *Catalysts* **2019**, *9*, 33. [[CrossRef](#)]
58. Riyapan, S.; Boonyongmaneerat, Y.; Mekasuwandumrong, O.; Yoshida, H.; Fujita, S.-I.; Arai, M.; Panpranot, J. Improved catalytic performance of Pd/TiO₂ in the selective hydrogenation of acetylene by using H₂-treated sol-gel TiO₂. *J. Mol. Catal. A Chem.* **2014**, *383–384*, 182–187. [[CrossRef](#)]

59. Akbayrak, S.; Tonbul, Y.; Özkaz, S. Nanoceria supported palladium (0) nanoparticles: Superb catalyst in dehydrogenation of formic acid at room temperature. *Appl. Catal. B Environ.* **2017**, *206*, 384–392. [[CrossRef](#)]
60. Zhang, H.; Sun, J.; Dagle, V.L.; Halevi, B.; Datye, A.K.; Wang, Y. Influence of ZnO facets on Pd/ZnO catalysts for methanol steam reforming. *ACS Catal.* **2014**, *4*, 2379–2386. [[CrossRef](#)]
61. Onderwaater, W.G.; Taranovsky, A.; van Baarle, G.C.; Frenken, J.W.M.; Groot, I.M.N. In Situ Optical Reflectance Difference Observations of CO Oxidation over Pd (100). *J. Phys. Chem. C* **2017**, *121*, 11407–11415. [[CrossRef](#)]
62. Ravishankar, T.N.; Vaz, M.D.O.; Ramakrishnappa, T.; Teixeira, S.R.; Dupont, J.; Pai, R.K.; Banuprakash, G. The heterojunction effect of Pd on TiO₂ for visible light photocatalytic hydrogen generation via water splitting reaction and photodecolorization of trypan blue dye. *J. Mater. Sci. Mater. Electron.* **2018**, *29*, 11132–11143. [[CrossRef](#)]
63. Caudillo-Flores, U.; Muñoz-Batista, M.J.; Fernández-García, M.; Kubacka, A. Bimetallic Pt-Pd co-catalyst Nb-doped TiO₂ materials for H₂ photo-production under UV and Visible light illumination. *Appl. Catal. B Environ.* **2018**, *238*, 533–545. [[CrossRef](#)]
64. Sokolov, S.; Ortel, E.; Kraehnert, R. Mesoporous titania films with adjustable pore size coated on stainless steel substrates. *Mater. Res. Bull.* **2009**, *44*, 2222–2227. [[CrossRef](#)]
65. Das, S.K.; Bhunia, M.K.; Bhaumik, A. Self-assembled TiO₂ nanoparticles: Mesoporosity, optical and catalytic properties. *Dalt. Trans.* **2010**, *39*, 4382–4390. [[CrossRef](#)] [[PubMed](#)]
66. Liu, S.-H.; Syu, H.-R. One-step fabrication of N-doped mesoporous TiO₂ nanoparticles by self-assembly for photocatalytic water splitting under visible light. *Appl. Energy* **2012**, *100*, 148–154. [[CrossRef](#)]
67. Yu, J.C.; Wang, X.; Fu, X. Pore-Wall Chemistry and Photocatalytic Activity of Mesoporous Titania Molecular Sieve Films. *Chem. Mater.* **2004**, *16*, 1523–1530. [[CrossRef](#)]
68. Wang, J.; Li, H.; Li, H.; Zou, C.; Wang, H.; Li, D. Mesoporous TiO₂ thin films exhibiting enhanced thermal stability and controllable pore size: Preparation and photocatalyzed destruction of Cationic Dyes. *ACS Appl. Mater. Interfaces* **2014**, *6*, 1623–1631. [[CrossRef](#)]
69. Salas, S.E.; de Lasa, H. Photocatalytic Water Splitting using a Modified Pt-TiO₂. Kinetic Modeling and Hydrogen Production Efficiency. Ph.D. Thesis, The University of Western Ontario, London, ON, Canada, 27 August 2013.
70. De Lasa, H.; Serrano, B.; Salaiques, M. *Photocatalytic Reaction Engineering*; Springer Science: New York, NY, USA, 2005.
71. Fagerlund, G. Determination of specific surface by the BET method. *Matér. Constr.* **1973**, *6*, 239–245. [[CrossRef](#)]
72. Slav, A. Optical characterization of TiO₂-Ge nanocomposite films obtained by reactive magnetron sputtering. *Dig. J. Nanomater. Biostruct.* **2011**, *6*, 915–920.
73. Guo, S.P.; Li, J.C.; Xu, Q.T.; Ma, Z.; Xue, H.G. Recent achievements on polyanion-type compounds for sodium-ion batteries: Syntheses, crystal chemistry and electrochemical performance. *J. Power Sources* **2017**, *361*, 285–299. [[CrossRef](#)]
74. Colmenares, J.C.; Lisowski, P.; Łomot, D.; Chernyayeva, O.; Lisovytskiy, D. Sonophotodeposition of Bimetallic Photocatalysts Pd-Au/TiO₂: Application to Selective Oxidation of Methanol to Methyl Formate. *ChemSusChem* **2015**, *8*, 1676–1685. [[CrossRef](#)]
75. Sanchez, C.; Boissière, C.; Grosso, D.; Laberty, C.; Nicole, L. Design, Synthesis, and Properties of Inorganic and Hybrid Thin Films Having Periodically Organized Nanoporosity. *Chem. Mater.* **2008**, *20*, 682–737. [[CrossRef](#)]
76. Ortel, E.; Polte, J.; Bernsmeier, D.; Eckhardt, B.; Paul, B.; Bergmann, A.; Strasser, P.; Emmerling, F.; Kraehnert, R. Pd/TiO₂ coatings with template-controlled mesopore structure as highly active hydrogenation catalyst. *Appl. Catal. A Gen.* **2015**, *493*, 25–32. [[CrossRef](#)]
77. Salaiques, M.; Serrano, B.; de Lasa, H. Photocatalytic Conversion of Organic Pollutants Extinction Coefficients and Quantum Efficiencies. *Ind. Eng. Chem. Res.* **2001**, *40*, 5455–5464. [[CrossRef](#)]

